



1

2 Enhanced understanding of atmospheric blocking modulation on ozone
3 dynamics within a high-resolution Earth system model

4 Wenbin Kou¹, Yang Gao^{1*}, Dan Tong², Xiaojie Guo^{3,4}, Xiadong An⁵, Wenyu Liu², Mengshi Cui²,
5 Xiuwen Guo¹, Shaoqing Zhang⁶, Huiwang Gao¹, Lixin Wu⁶

6

7 ¹Frontiers Science Center for Deep Ocean Multispheres and Earth System and Key Laboratory of
8 Marine Environmental Science and Ecology, Ministry of Education, Ocean University of China,
9 and Laoshan Laboratory, Qingdao, 266100, China

10 ²Department of Earth System Science, Tsinghua University, Beijing, 100084, China

11 ³International Center for Climate and Environment Sciences, Institute of Atmospheric Physics,
12 Chinese Academy of Sciences, Beijing, 100029, China

13 ⁴University of Chinese Academy of Sciences, Beijing, 100049, China

14 ⁵College of Oceanic and Atmospheric Sciences, Ocean University of China, Qingdao, 266100,
15 China

16 ⁶Frontiers Science Center for Deep Ocean Multispheres and Earth System, and Key Laboratory of
17 Physical Oceanography, Ministry of Education, the College of Oceanic and Atmospheric Sciences,
18 Ocean University of China, and Laoshan Laboratory, Qingdao, 266100, China

19

20 *Correspondence to: yanggao@ouc.edu.cn

21

22

23

24

25

26

27

28

29

30



31

Abstract

32 High concentrations of surface ozone pose significant health risks, yet
33 understanding the factors governing ozone levels, particularly the influence of large-
34 scale circulations, remains incomplete. A key challenge lies in accurately modeling both
35 large-scale circulations and ozone concentrations. Leveraging recent advancements in
36 optimizing a high-resolution Earth system model with 25 km atmospheric resolution,
37 how local meteorology and large-scale circulations impact ozone concentrations is
38 investigated. We find that heatwaves can trigger substantial increases in ozone
39 concentrations by stimulating biogenic volatile organic compound (BVOC) emissions
40 during the summers of 2015-2019. For example, compared to non-heatwave periods,
41 ozone concentrations during heatwaves increase by 12.0 ppbv in the southeastern U.S.,
42 9.7 ppbv in Europe, 17.6 ppbv in North China, and 9.0 ppbv in central eastern China.
43 In addition to local effects, atmospheric blocking strongly influences downstream
44 meteorological conditions and ozone formation. Focusing on ozone pollution in eastern
45 China, we identify three major pathways of Rossby wave propagation based on
46 blocking locations: the Euro-Atlantic sector, northern Russia, and the North Pacific,
47 inducing increased air temperature and intensified downward surface solar radiation
48 downstream. The impact of blocking is most pronounced over central eastern China,
49 where ozone concentrations during blocking increase by 5.9 ppbv to 10.7 ppbv
50 compared to reference periods, followed by North China, ranging from 2.1 ppbv to 4.9
51 ppbv. Blocking can stimulate more BVOC emissions, enhancing ozone concentrations
52 by 10.6 ppbv to 15.9 ppbv. These findings underscore the critical role that large-scale
53 atmospheric circulation patterns play in regional-scale air quality, particularly under a
54 warming climate.

55

56 Key words: atmospheric blocking, ozone, Rossby wave propagation, BVOC emissions

57

58

59



60

Summary

61 Unlike traditional numerical studies, we apply a high-resolution Earth system model,
62 improving simulations of ozone and large-scale circulations such as atmospheric
63 blocking. In addition to local heatwave effects, we quantify the impact of atmospheric
64 blocking on downstream ozone concentrations, which is closely associated with the
65 blocking position. We identify three major pathways of Rossby wave propagation,
66 stressing the critical role of large-scale circulation play in regional air quality.

67



68 **1. Introduction**

69 Air pollution ranks as the fourth leading global risk factor for mortality, trailing high
70 systolic blood pressure, tobacco use, and dietary risks (Brauer et al., 2021). Among
71 atmospheric pollutants, ambient ozone is a major contributor to this burden (Fuller et
72 al., 2022), affecting human health (Nuvolone et al., 2018), global climate (Deitrick and
73 Goldblatt, 2023), and ecosystem health through exacerbating crop yield losses
74 (Emberson et al., 2018).

75 The HTAP (Hemispheric Transport of Air Pollution; Dentener et al., 2010; Parrish
76 et al., 2012) and TOAR (Tropospheric Ozone Assessment Report; Tarasick et al., 2019)
77 programs have extensively studied long-term ozone trends. Their synthesis in 2021
78 (Parrish et al., 2021b) reveals a twofold increase in lower tropospheric ozone at northern
79 mid-latitudes from 1950 to 2000. The World Health Organization (WHO) strengthened
80 air quality standards in 2021, emphasizing the critical need to assess ozone trends and
81 their key drivers.

82 Ozone, a secondary air pollutant, forms when emission precursors such as volatile
83 Organic Compounds (VOCs) and NO_x are present (Fu and Tian, 2019). While
84 anthropogenic emissions are significant, biogenic VOC (BVOC) emissions, which
85 comprise about 90% of global VOC emissions (Guenther et al., 2012), are particularly
86 sensitive to temperature. For instance, BVOC emissions notably elevate surface ozone
87 levels in the North China Plain, contributing to increases of 7.8 ppbv and 10.0 ppbv in
88 the regional average MDA8 ozone concentrations in the North China Plain and Beijing,
89 respectively, during the summer of 2017 (Ma et al., 2019). Even in less polluted regions
90 such as the U.S., BVOC emissions contribute a notable fraction of ozone, averaging 10%
91 and 19% in the western and southeastern U.S., respectively (Zhang et al., 2017).

92 This effect is amplified under favorable meteorological conditions. Compared to
93 non-heatwave periods, heatwaves trigger increased BVOC emissions, resulting in
94 regional daytime ozone concentration increases of 10 $\mu\text{g m}^{-3}$ in the Pearl River Delta,
95 with peaks reaching 42.1 $\mu\text{g m}^{-3}$ (Wang et al., 2021). In southwestern Europe,
96 heatwaves induce a 33% rise in BVOC emissions, resulting in surface ozone



97 concentration increases of $9 \mu\text{g m}^{-3}$ during the summers of 2012-2014 (Guion et al.,
98 2023). However, biases in modeling heatwaves (Gao et al., 2012) and ozone, such as
99 overestimations up to 20 ppbv in low-resolution global models (Emmons et al., 2020;
100 Lamarque et al., 2012), have hindered previous investigations, primarily conducted
101 using regional weather and chemistry models (Gao et al., 2020; Zhang et al., 2022).
102 Addressing these challenges, especially the biases from low-resolution global models
103 in boundary conditions (Zeng et al., 2022), is crucial for advancing Earth system models
104 to better understand the impact of heatwaves on ozone through BVOC emissions.

105 Local meteorological factors, particularly high temperatures, are closely linked to
106 large-scale circulations (Li and Sun, 2018), which further influence the ozone-
107 temperature relationship. For instance, the correlation between summer surface ozone
108 and temperature over eastern North America correlates with the position of the jet
109 stream, defined by the latitude of the maximum 500 hPa zonal wind averaged across
110 the region (Barnes and Fiore, 2013). Atmospheric circulations, such as the North
111 Atlantic Oscillation, significantly affect moisture transport, precipitation, and
112 subsequently, trace gas transport, deposition and air pollutant concentrations
113 (Christoudias et al., 2012). In central eastern China, the East Asian summer monsoon
114 explains 2%-5% of interannual variations in surface ozone concentrations (Yang et al.,
115 2014). Moreover, a positive phase of the Eurasian teleconnection induces Rossby wave
116 train propagation from Europe to North China, influencing downward surface solar
117 radiation intensity and temperatures, thereby modulating ozone concentration
118 variability (Yin et al., 2019).

119 Recently, Yang et al. (2022) highlighted that high temperatures alone may not
120 always enhance ozone formation.. For instance, high temperatures induced by a zonal
121 '+ - +' wave-train pattern over Eurasia at 300 hPa may not favor ozone enhancement in
122 North China. In contrast, circulation anomalies resembling an atmospheric blocking
123 pattern, including positive geopotential height anomalies at 300 hPa over North China
124 and eastern Eurasia, can lead to weaker meridional temperature gradients, intensified
125 downward solar radiation, reduced cloud cover, and aggravated ozone pollution.



126 Atmospheric blocking, a quasi-stationary, large-scale extra-tropical weather system,
127 often occurs over expansive regions like the North Atlantic-Europe and North Pacific
128 (Pelly and Hoskins, 2003; Schwierz et al., 2004; Woollings et al., 2018). Blocking highs
129 are frequently associated with extreme weather events (Barriopedro et al., 2011;
130 Cattiaux et al., 2010). For example, through downstream Rossby wave propagation
131 from Alaska to East Asia, Alaska blocking can induce subsequent blocking over the
132 Urals, influencing extreme cold events across North America and Eurasia (Yao et al.,
133 2023).

134 Despite significant advancements, the impact of atmospheric blocking on extreme
135 weather events and ozone remains insufficiently explored. For example, using a
136 Hovmöller diagram and local wave activity calculated from 500 hPa geopotential height,
137 Sun et al. (2019) found that variations in wave activity can explain 30-40% of ozone
138 variability in historical U.S. summers. Challenges in global models, such as simulated
139 biases in atmospheric blocking and ozone, including overestimations (Clifton et al.,
140 2020), have undermined confidence in linking large-scale circulation patterns with
141 ozone levels (Barnes and Fiore, 2013).

142 Building on recent advances in high-resolution Earth system models that mitigate
143 ozone biases (Gao et al., in review-b) and simulate meteorological parameters and
144 climate extremes (Chang et al., 2020; Gao et al., in review-a; Gao et al., 2023; Guo et
145 al., 2022), this study is structured as follows. Section 2 describes the model setup. It is
146 followed by an analysis of observational ozone data, the effects of BVOC emissions,
147 and heatwaves on ozone concentrations. Finally, we explore how atmospheric blocking
148 influences ozone pollution in eastern China.

149

150 **2 Method and data**

151 **2.1 Model configurations**

152 In this study, we utilize the Community Earth System Model version 1.3,
153 employing the Community Atmosphere Model 5.0 (CAM5) as its atmospheric
154 component. CAM5 runs at two spatial resolutions: nominal 1° and 0.25°. Sea surface



155 temperature and sea ice are prescribed at a spatial resolution of of $1.0^\circ \times 1.0^\circ$.
156 Atmospheric gas chemistry and aerosol processes are simulated using the Model for
157 OZone And Related chemical Tracers (MOZART) and the three-mode version of the
158 Modal Aerosol Module (MAM3). The high-resolution and low-resolution
159 configurations of CESM are denoted as SW-HRESM and CESM-LR, respectively.
160 Further details can be found in Gao et al. (in review-b). The simulation period covers
161 June to August from 2015 to 2019, with May used for spin-up to mitigate initial
162 condition influences.

163 Emissions for the simulations are sourced as follows: anthropogenic emissions
164 from the Copernicus Atmosphere Monitoring Service global emissions (CAMS-
165 GLOB-ANT v4.2-R1.1; Granier et al., 2019), with updates for China based on the
166 Multi-resolution Emission Inventory for China (MEIC; Li et al., 2017). Volcanic
167 emissions are from Global Emission Inventory Activity (GEIA), and aircraft emissions
168 from the Community Emission Data System (CEDS). Biomass burning emissions data
169 are sourced from the Fire INventory from National Center for Atmospheric Research
170 (FINN) version 2.5 (Wiedinmyer et al., 2023). High-resolution simulations use
171 emissions data at 0.1° resolution, while low-resolution simulations aggregate emissions
172 from 0.1° to $\sim 1.0^\circ$ resolution. Biogenic emissions are calculated online using the Model
173 of Emissions of Gases and Aerosols from Nature version 2.1 (MEGAN2.1; Guenther et
174 al., 2012). Further emission details are available in Gao et al. (in review-b).

175 Two numerical experiments are designed to assess the impact of BVOC emissions
176 on ozone. The first experiment includes all emissions (BASE case), while the second
177 experiment turns off BVOC emissions (No_BVOC case). By subtracting results from
178 the No_BVOC case from those of the BASE case, we isolate the contribution of BVOC
179 emissions to ozone.

180

181 **2.2 Blocking detection method and Rossby wave flux calculation**

182 To identify atmospheric blocking, we use a two-dimensional hybrid blocking index
183 based on 500 hPa geopotential height. The index is applied across a range of latitudes,



184 ϕ , (40° to 75° N) for each longitude, λ , incorporating meridional gradients to
 185 identify blocked grid points:

$$186 \quad GHGN(\lambda, \phi) = \frac{Z(\lambda, \phi + \Delta) - Z(\lambda, \phi)}{\Delta} < -10,$$

$$187 \quad GHGS(\lambda, \phi) = \frac{Z(\lambda, \phi) - Z(\lambda, \phi - \Delta)}{\Delta} > 0,$$

$$188 \quad Z_{\text{anomaly}}(\lambda, \phi) = Z(\lambda, \phi) - \bar{Z}(\phi) > 0,$$

189 where, GHGN (GHGS) indicates the meridional gradient to the north (south) of
 190 geopotential height at 500 hPa, Z means the 500 hPa geopotential height at longitude
 191 λ along latitude ϕ , and \bar{Z} is the zonal (0° to 360°) average of Z at latitude ϕ ; Δ is
 192 set as 15°.

193
 194 A blocking region is defined when the meridional extension of blocked grid points
 195 exceeds 15°. The center of each blocking region is determined as the grid point with
 196 maximal 500 hPa geopotential height. Sequential blocking events are identified if the
 197 center of a blocking region on one day was within a specified distance (27° in latitude
 198 × 36° in longitude) of the center on the previous day. We restrict a blocking event lasting
 199 at least five days. More information can be found in Masato et al. (2013) and Gao et al.
 200 (in review-a).

201 To examine Rossby wave propagation, the horizontal stationary wave activity flux
 202 (\mathbf{W}) is calculated following Takaya and Nakamura (2001). Key variables used for flux
 203 calculation include zonal wind (U), meridional wind (V), wind speed ($|\mathbf{U}|$), and
 204 anomalous geopotential height (Φ').

$$205 \quad \mathbf{W} = \frac{P \cos \phi}{2|\mathbf{U}|} \cdot \left(\begin{array}{l} \frac{U}{a^2 \cos^2 \phi} \left[\left(\frac{\partial \psi'}{\partial \lambda} \right)^2 - \psi' \frac{\partial^2 \psi'}{\partial \lambda^2} \right] + \frac{V}{a^2 \cos \phi} \left[\frac{\partial \psi'}{\partial \lambda} \frac{\partial \psi'}{\partial \phi} - \psi' \frac{\partial^2 \psi'}{\partial \lambda \partial \phi} \right] \\ \frac{U}{a^2 \cos \phi} \left[\frac{\partial \psi'}{\partial \lambda} \frac{\partial \psi'}{\partial \phi} - \psi' \frac{\partial^2 \psi'}{\partial \lambda \partial \phi} \right] + \frac{V}{a^2} \left[\left(\frac{\partial \psi'}{\partial \phi} \right)^2 - \psi' \frac{\partial^2 \psi'}{\partial \phi^2} \right] \end{array} \right), \quad (1)$$

206 where \mathbf{W} represents the wave activity flux (unit: $\text{m}^2 \text{s}^{-2}$), ψ' ($= \Phi'/f$) represents the
 207 geostrophic stream function, $f (= 2\Omega \sin \phi)$ is the Coriolis parameter, P is the normalized
 208 pressure (P per 1000 hPa), and a is Earth's radius. λ and ϕ denote the longitude and



209 latitude, respectively.

210

211 **2.3 Observational data**

212 Observational ozone data are collected from several platforms, including the Air
213 Quality System (AQS, <https://www.epa.gov/aqs>; last access: 30 June, 2023) and the
214 Clean Air Status and Trends Network (CASTNET, <https://www.epa.gov/castnet>; last
215 access: 30 April, 2023) in the U.S., the European Monitoring and Evaluation
216 Programme database (EMEP; <http://ebas.nilu.no>; last access: 30 January 2023) in
217 Europe, and the China National Environmental Monitoring Center (CNEMC,
218 <http://www.pm25.in>; last access: December 8, 2021) in China. The monitoring network
219 comprises 1293 sites for AQS, 99 for CASTNET, 286 for EMEP and 2025 for CNEMC.
220 Meteorological data used in this study are sourced from the National Centers for
221 Environmental Prediction's Reanalysis-1 (NCEP; Kalnay et al., 1996).

222

223 **3 Results and discussion**

224 **3.1 Characteristics of observed ozone in the Northern Hemisphere**

225 Fig. 1 illustrates the characteristics of observed ozone levels based on a
226 comprehensive analysis of extensive observational datasets. Peak season ozone (Fig.
227 1a), as defined by the WHO in 2021, is determined using a 6-month running average of
228 maximum daily 8-h (MDA8) ozone concentrations for each grid, with the maximum
229 value being considered. The WHO air quality guideline is set at $60 \mu\text{g}\cdot\text{m}^{-3}$ (31 ppbv),
230 with additional standards of $100 \mu\text{g}\cdot\text{m}^{-3}$ (51 ppbv) and $70 \mu\text{g}\cdot\text{m}^{-3}$ (36 ppbv). Regional
231 differences in ozone pollution are apparent: higher concentrations are observed in the
232 western U.S. due to elevated altitude and background levels (Parrish et al., 2021a).
233 Specific sites with significant ozone pollution include L.A. and Houston, as previously
234 documented (Dunker et al., 2017). In Europe, ozone pollution is more pronounced in
235 southern regions, particularly around the Mediterranean, consistent with earlier studies
236 (Zohdirad et al., 2022). In China, the eastern region exhibits concentrated pollution.
237 Mean peak season ozone levels are 45.5 ppbv in the U.S., 42.9 ppbv in Europe, and

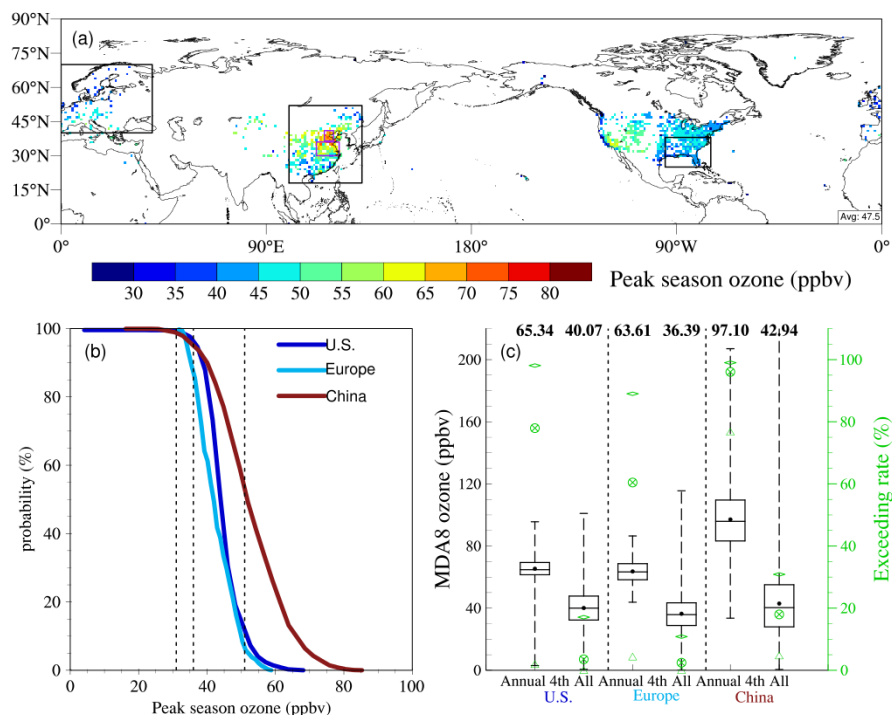


238 53.7 ppbv in China.

239 The cumulative distribution function of peak season ozone concentrations is
240 shown in Fig. 1b using gridded data. In the U.S. and Europe, only 15% and 8% of the
241 peak season ozone concentrations, respectively, exceed the level I (51ppbv) from 2015
242 to 2019, whereas in China, almost 60% exceed this threshold. However, when applying
243 the stricter standard (36ppbv), exceedance rates are notably high: 98%, 89%, and 96%
244 in the U.S., Europe and China, respectively.

245 Fig. 1c presents the fourth highest MDA8 ozone values annually from 2015 to
246 2019, alongside daily values for the U.S., Europe and China. The WHO has established
247 standards at 82 ppbv and 61 ppbv, with an air quality guideline of 51ppbv. Exceedance
248 rates for the strictest guideline (51 ppbv) are 98%, 89% and 99% in the U.S., Europe
249 and China, respectively. For the 61ppbv standard, rates are 78%, 60% and 96%,
250 respectively, and for the 82ppbv standard, exceedance rates are 2%, 4% and 77%,
251 respectively. Considering all daily values, with a sample size approximately 365 times
252 larger than the annual fourth highest value, the rates of ozone exceedance (i.e.,
253 exceeding 51 ppbv) are observed to be 17% in the U.S., 11% in Europe, and 31% in
254 China. This indicates that there are significantly more days where ozone levels exceed
255 the threshold beyond just the fourth highest maximum daily 8-hour (MDA8) ozone
256 level in these regions. This suggests that air quality issues related to ozone are more
257 persistent and widespread than what might be inferred solely from the fourth highest
258 MDA8 metric.

259



260

261 **Fig. 1 Peak season ozone concentrations and maximum daily 8-hr (MDA8) ozone**
 262 **concentrations.** (a) Spatial distribution of mean peak season ozone concentrations in
 263 the Northern Hemisphere from 2015 to 2019. The black squares represent regions in
 264 Europe, eastern China, and the U.S., while the purple squares in eastern China denote
 265 North China and central eastern China regions. (b) Cumulative Distribution Function
 266 of peak season ozone concentrations, with dashed lines indicating WHO standard
 267 values (31 ppbv, 36 ppbv, 51 ppbv) set by WHO. (c) Box-and-whisker plot of annual
 268 fourth-highest (left) and all (right) MDA8 during 2015-2019 in the U.S., Europe and
 269 China. The boxes represent the interquartile range (25th to 75th percentiles), horizontal
 270 lines denote medians, solid points indicate averages, and line end points show
 271 maximum and minimum values. Exceedance rates (%) of MDA8 to WHO standards of
 272 82 ppbv, 61 ppbv, and 51 ppbv are marked with green triangle, crossed-out circle, and
 273 diamond symbols, respectively.

274

275



276 **3.2 BVOC emissions and their effects on ozone**

277 BVOC emissions during the summer months of 2015-2019 are depicted in Fig. 2a
278 and Fig. 2b, with global totals of 86.0 Tg month⁻¹ in SW-HRESM and 90.7 Tg month⁻¹
279 in CESM-LR. Isoprene emissions (Fig. 2c, d) account for nearly half of these totals
280 amounting to 42.3 Tg month⁻¹ in SW-HRESM and 45.2 Tg month⁻¹ in CESM-LR. This
281 predominance of isoprene emissions aligns with previous studies (Ma et al., 2022;
282 Mochizuki et al., 2020). Isoprene emissions are predominantly concentrated in tropical
283 regions, reflecting the prevalence of dense forest cover. Our study indicates values
284 approximately 30% higher than those (Fig. S1) reported in Weng et al. (2020) due to
285 previously underestimated emissions in tropical regions.

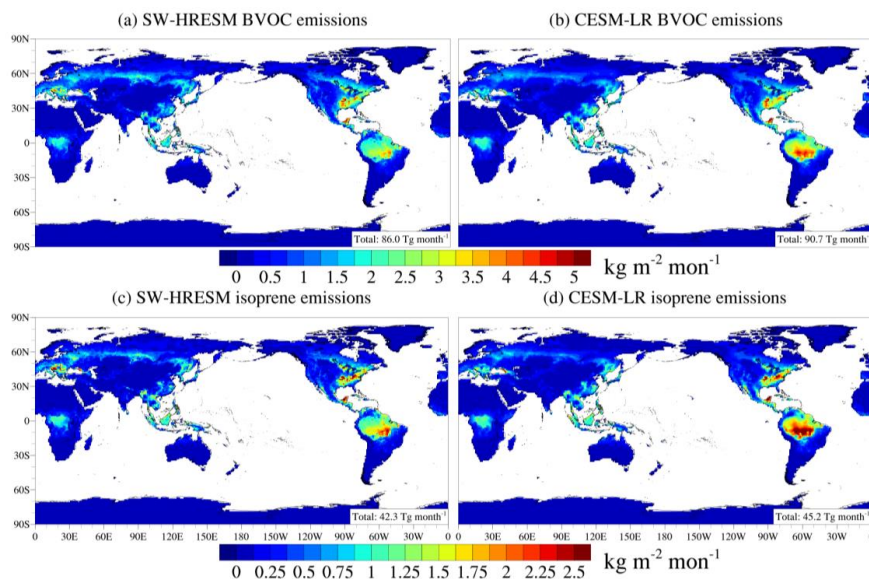
286 To assess the utility of high-resolution simulations, we compute the standard
287 deviation across 16 grid points in SW-HRESM corresponding to a single low-resolution
288 grid (Fig. S2). The average monthly isoprene emissions during 2015-2019 are 0.63 kg
289 m⁻², 0.51 kg m⁻² and 0.21 kg m⁻² over the U.S., Europe and China (Fig. 2c), respectively,
290 with mean standard deviation of 0.13 kg m⁻², 0.11 kg m⁻², 0.05 kg m⁻² (Fig. S2). This
291 ratio also applies to biogenic emission-rich areas such as the southeastern U.S., southern
292 Europe and eastern China, highlighting the importance of using finer grid spacings for
293 accurately capturing the spatial heterogeneity of BVOC emissions.

294 The spatial distribution of BVOC emissions closely correlates with the distribution
295 of broadleaf trees (Fig. S3), which have higher emission factors compared to other plant
296 types (Table 2 in Guenther et al., 2012). Isoprene emissions are most intense in tropical
297 regions where broadleaf evergreen and deciduous tropical trees predominate, as well as
298 in mid-to-high latitude belts and isolated hotspots in mid-latitudes like the southeastern
299 U.S., southern Europe, and eastern China.

300 An exception is observed in the Amazon region, where despite dense broad
301 evergreen tropical forest cover, the largest isoprene and BVOC emissions occur away
302 from the main forest area. This Amazon hotspot, noted in previous studies (Opacka et
303 al., 2021), is influenced by key meteorological factors such as 2-meter air temperature
304 and downward surface solar radiation (Fig. S4). Specifically, areas with higher



305 temperatures and stronger solar radiation exhibit greater BVOC and isoprene emissions.
306 The discrepancy in temperature between CESM-LR and SW-HRESM simulations
307 reveals nuances in emission patterns, with CESM-LR showing slightly higher
308 temperatures that lead to increased emissions. The slightly lower temperature in higher
309 grid spacing simulations in regional climate model was also reported by Pugh et al.
310 (2013). They suggested that improved representation of forests could increase latent
311 heat flux and thereby mitigate temperature rises through a reduced sensible heat. The
312 study compared three grid spacings: 0.1°, 0.5°, and 2.0°, showing that across regions
313 such as South America, Southeast Asia, and the southeastern U.S., there was a small
314 overall difference of about 2% in BVOC emissions on a regional scale. However, this
315 difference could reach up to 150% in high-emission areas.



316
317 **Fig. 2 Spatial distribution of BVOC (top) and isoprene (bottom) emissions based**
318 **on SW-HRESM (left) and CESM-LR (right).** Shown are monthly total emissions
319 averaged during the summer of 2015-2019.

320
321 To understand the contribution of BVOC emissions to ozone concentrations across
322 different grid resolutions, we compare two scenarios: one with biogenic emissions

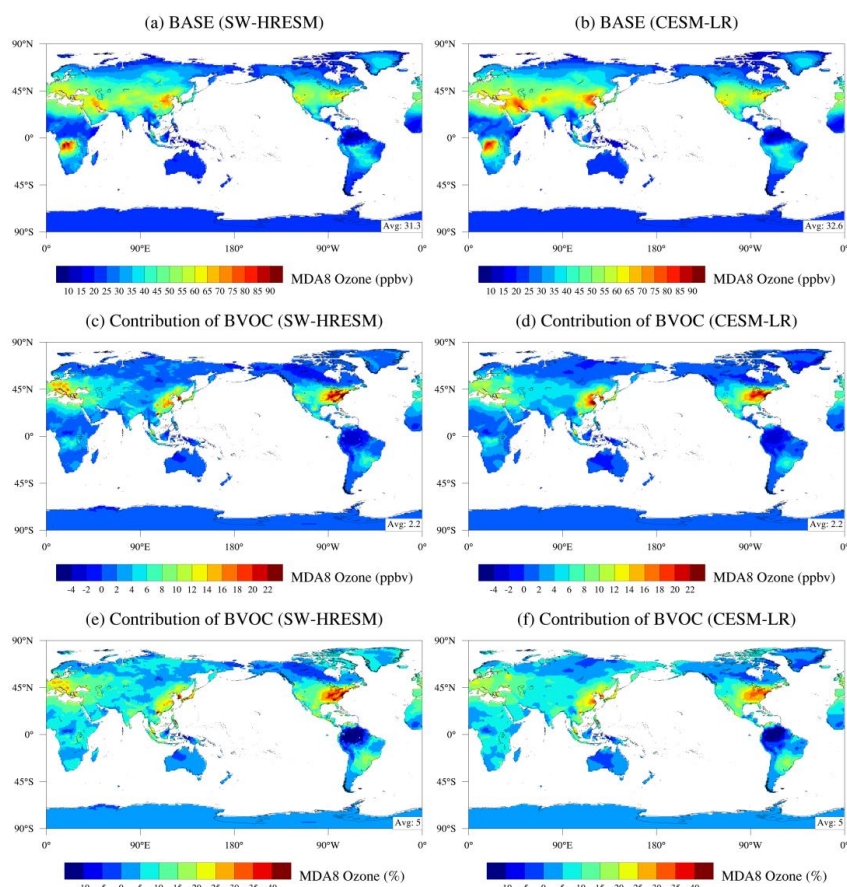


323 included and one without. Fig. 3a and 3b illustrate the spatial distribution of ozone
324 concentrations averaged over the summers of 2015-2019 for both SW-HRESM and
325 CESM-LR. Both models identify significant ozone pollution areas in the Northern
326 Hemisphere, particularly over southern Europe, the southeastern U.S., and eastern
327 China. The contribution of BVOC emissions to ozone concentrations is further detailed
328 in Fig. 3c-f.

329 In SW-HRESM, BVOC emissions contribute approximately 2.2 ppbv to the global
330 mean ozone concentrations over land, representing 7% relative to the mean value of
331 31.3 ppbv (Fig. 3c,e). However, the impact of BVOC emissions on ozone
332 concentrations is modulated by factors such as anthropogenic emissions and
333 meteorological conditions. Regions with abundant BVOC emissions and higher ozone
334 concentrations, such as the U.S., Europe, and eastern China, show a substantial
335 contribution of 15% to 30% from BVOC emissions to ozone levels. In contrast, the
336 Amazon rainforest in Brazil, despite having the highest BVOC emissions, exhibits a
337 negative contribution to ozone levels. This is attributed to the fact that in regions with
338 low NO_x concentrations, increased VOCs initiated by OH oxidation can lead to the
339 formation of stable organic nitrogen compounds, through increasing organic peroxy
340 radicals and elevating the reaction with NO₂ (Tonnesen and Jeffries, 1994). It reduces
341 the availability of NO₂ and the subsequent photolysis such as a reduction of O₃P,
342 thereby reducing ozone concentrations (Kang et al., 2003; Unger, 2014). While this
343 effect is evident in CESM-LR, lower resolution simulations may overlook finer-scale
344 variability, affecting the accuracy of quantifying the impact of BVOC emissions on
345 ozone.

346

347



348

349 **Fig. 3 Spatial distribution of MDA8 ozone from SW-HRESM (left) and CESM-LR**
350 **(right).** Shown are results of ozone concentrations at BASE (top) and the contribution
351 of BVOC emissions to ozone (middle row: ppbv; bottom row: %). Global mean values
352 over land are indicated in the bottom right.

353

354 3.3 Effects of heatwaves on ozone

355 Heatwaves not only accelerate photochemical reactions but also intensify BVOC
356 emissions, thereby amplifying ozone production and exacerbating ozone pollution.
357 Building on previous studies (Gao et al., 2012; Sillmann et al., 2013), heatwaves are
358 defined within each grid as periods when the daily mean near-surface air temperature
359 exceeds the 90th percentile of the climatological mean, focusing on the summer period



360 from 2015 to 2019 in this study. To quantify the impact of heatwaves on ozone
361 concentrations, Fig. 4 illustrates the probability distribution function (PDF) of MDA8
362 ozone concentrations for both the BASE case and a scenario without BVOC emissions,
363 aggregated across entire summer periods and specifically during heatwave days. Given
364 the superior capability of high-resolution simulations in reproducing heatwaves and
365 ozone concentrations (Gao et al., in review-b; Gao et al., 2023), we present results
366 solely from SW-HRESM hereafter.

367 Several notable observations emerge. Firstly, a comparison of heatwave periods to
368 non-heatwave periods (solid red vs. solid blue lines in Fig. 4) reveals a noticeable
369 rightward shift in the PDF, indicating an increase in ozone levels due to heatwave
370 impacts, a well-established phenomenon (e.g., Gao et al., 2020; Zhang et al., 2018).
371 Specifically, compared to non-heatwave periods, mean ozone concentrations increase
372 by 9.1 ppbv, 9.7 ppbv, and 8.4 ppbv during heatwaves over the U.S., Europe, and eastern
373 China, respectively. This effect is more pronounced in specific regions, such as North
374 China (NC) with an increase of 17.6 ppbv, followed by the southeastern U.S. (12.0 ppbv)
375 and central eastern China (CECN) (9.0 ppbv), accounting for 12% to 21% of regional
376 mean ozone levels. A previous study noted that median surface ozone concentrations
377 during U.S. heatwaves from 1990 to 2016 could increase by 10% to 80% (Meehl et al.,
378 2018).

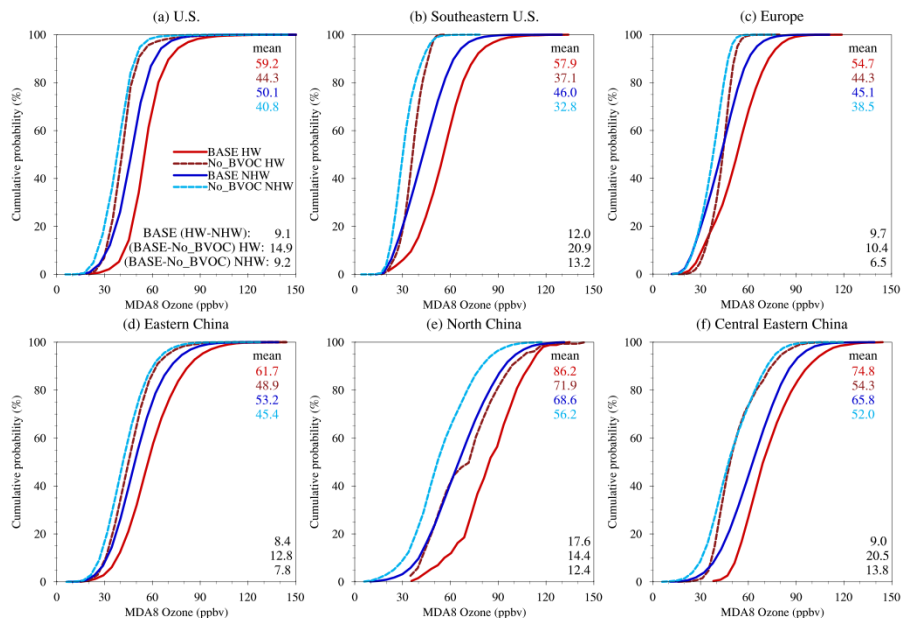
379 Comparing scenarios with and without BVOC emissions (solid vs. dashed lines in
380 Fig. 4), BVOC emissions significantly contribute to ozone enhancement during both
381 non-heatwave and heatwave periods. For instance, during heatwaves, BVOC emissions
382 contribute 20.9 ppbv, 10.4 ppbv, 14.4 ppbv, and 20.5 ppbv over the southeastern U.S.,
383 Europe, North China, and central eastern China, respectively. A study by Churkina et
384 al. (2017) found that biogenic emissions contributed 17-20% to ozone formation in
385 Berlin, Germany, in July 2006, with this contribution potentially increasing to 60%
386 during heatwaves.

387 It is important to note that the influence of BVOC emissions persists outside of
388 heatwave periods, particularly when downward surface solar radiation remains



389 sufficiently high (Fig. S5). The differences in BVOC contributions to ozone between
 390 heatwave and non-heatwave periods represent the incremental effect of BVOCs during
 391 heatwaves, accounting for 7.7 ppbv, 3.9 ppbv, 2.0 ppbv, and 6.7 ppbv over these four
 392 regions, respectively. This incremental effect constitutes 64%, 40%, 11%, and 74% of
 393 the total heatwave effects, indicating varying degrees of BVOC influence across
 394 different regions. The relatively smaller incremental BVOC effect during heatwaves
 395 over North China is partly attributed to higher anthropogenic emissions and lower
 396 BVOC emissions compared to the other regions. With potential reductions in
 397 anthropogenic emissions in China, BVOC emissions could assume a more pivotal role,
 398 especially given projections of increased frequency of heatwaves in a warming climate
 399 (Gao et al., 2023; Gao et al., 2022).

400



401

402 **Fig. 4 Cumulative Density Function (CDF) of MDA8 ozone concentrations.** Shown
 403 are results for the BASE case (solid line) and the case without BVOC emissions (dashed
 404 line), during heatwaves (red) and non-heatwaves (blue) based on SW-HRESM.

405

406



407 **3.4 The role of atmospheric blocking on ozone pollution in eastern China**

408 Eastern China has emerged as a significant region grappling with severe ozone
409 pollution. Numerous studies have endeavored to explore the driving factors,
410 particularly in the last decade, leveraging the widespread availability of ozone data
411 across China. For example, through the examination of ozone pollution events in North
412 China during 2014-2017, Gong and Liao (2019) investigated ozone pollution episodes
413 in North China from 2014 to 2017 and identified that under weather conditions
414 characterized by high near-surface air temperatures, low relative humidity, and
415 anomalous southerly winds in the lower troposphere, ozone concentrations tend to
416 accumulate in this region. Mousavinezhad et al. (2021) utilized a multiple linear
417 regression model to disentangle the contributions of meteorology and emissions to
418 ozone levels in North China during 2015-2019. Their findings indicated that
419 meteorological factors such as increased downward surface solar radiation and near-
420 surface air temperatures accounted for 32% of the observed ozone increase, while
421 changes in emission precursors contributed 68%. To elucidate the interannual
422 variability of ozone in North China, Gong et al. (2020) employed tagged O₃ simulations
423 with the Goddard Earth Observing System Chemical Transport Model (GEOS-Chem)
424 model and suggested that one-third of the rise in ozone pollution days observed from
425 2014 to 2018, particularly in 2018, could be attributed to emissions transport from
426 central-eastern China. Considering the intertwined roles of meteorology and emissions,
427 the focus shifted to examining ozone anomalies relative to their respective monthly
428 averages, thereby minimizing the influence of emissions on ozone variability.

429 The study focuses on two specific regions—North China and central eastern
430 China—to analyze days where regional mean MDA8 ozone levels exceeded 10 ppbv
431 of their respective monthly means, defined as regional ozone pollution events.
432 Observational data indicate a total of 131 and 89 such events in North China and central
433 eastern China, respectively, during the summers of 2015-2019. Ozone pollution events
434 are observed to extend meridionally (Figs. 5,6), northward into northeastern China from
435 North China (Fig. 5a,b) and covering large areas of northern and southern China from

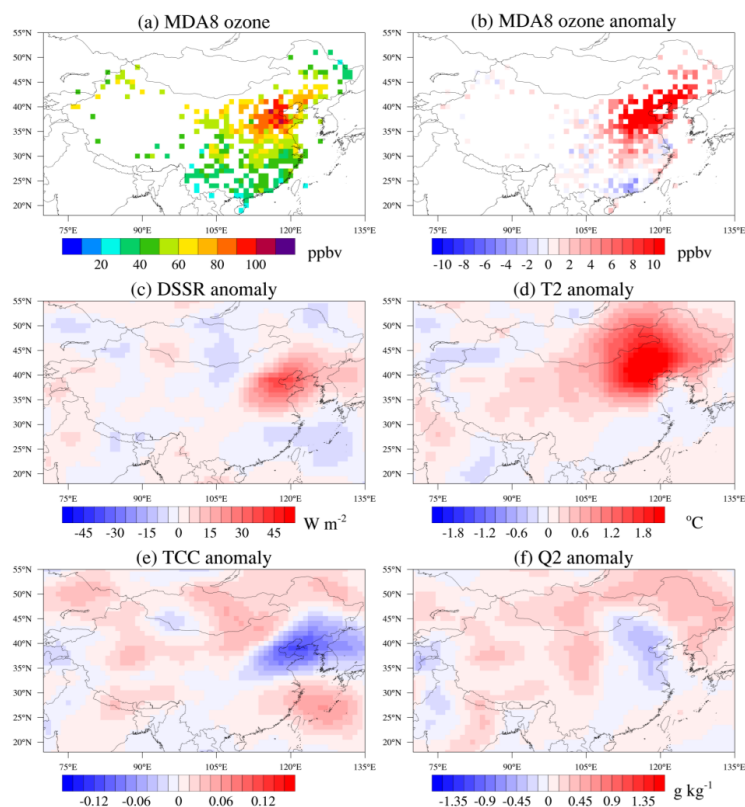


436 central eastern China (Fig. 6a,b).

437

438 During regional ozone pollution events, concurrent meteorological conditions
439 typically feature higher downward surface solar radiation, 2-meter air temperatures,
440 reduced water vapor, and decreased total cloud cover, all of which favored ozone
441 accumulation. Meteorological anomalies for each day are computed relative to their
442 respective months, with the study testing four different methods for deriving
443 climatology, including averages from the same day, same month, summer periods from
444 2015-2019, and summers from 1990-2019. They all yield comparable results.
445 Analyzing atmospheric blocking, we find that 43% (56 events) of regional ozone
446 pollution events in North China and 48% (43 events) in central eastern China are
447 accompanied by blocking. Notably, among the 36 events where ozone pollution
448 concurrently affected both North China and central eastern China, nearly 40% are
449 associated with blocking events.

450



451

452 **Fig. 5 Spatial distributions of ozone and meteorological conditions during ozone**

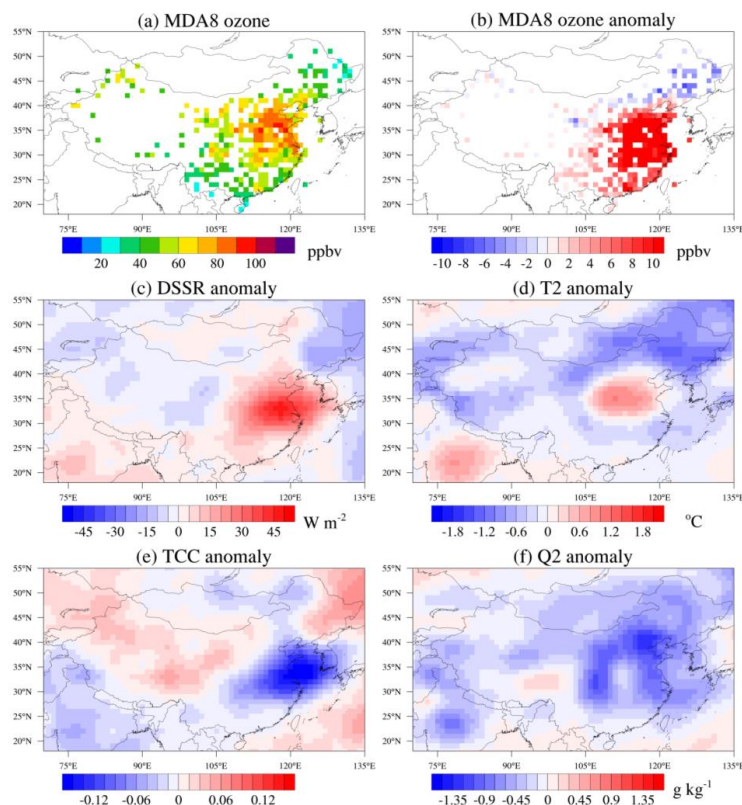
453 **pollution events in North China.** Shown are composited results of (a) mean MDA8

454 ozone concentrations, anomalies of (b) MDA8 ozone, (c) downward surface solar

455 radiation, (d) 2-m air temperature, (e) total cloud cover, and (f) 2-m specific humidity

456 during the summers of 2015-2019.

457



458

459 **Fig. 6 Spatial distributions of ozone and meteorological conditions during ozone**
460 **pollution events in central eastern China.** Shown are composited results of (a) mean
461 MDA8 ozone concentrations, anomalies of (b) MDA8 ozone, (c) downward surface
462 solar radiation, (d) 2-m air temperature, (e) total cloud cover, and (f) 2-m specific
463 humidity during the summers of 2015-2019.

464

465 The impact of blocking events on downstream meteorological conditions and ozone
466 pollution is examined, primarily based on Rossby wave propagation, which profoundly
467 affects large-scale circulations. For example, Ding and Li (2017) analyzed reanalysis
468 data from 1951–2015 and found that Rossby waves originating from northwest Europe
469 entered the North Africa-Asia westerly jet in the upper troposphere, propagating
470 eastward along the subtropical westerly jet. This circulation favored persistent heavy
471 rainfall events in South China (20°-30°N). Liu et al. (2022) studied data from 1979–



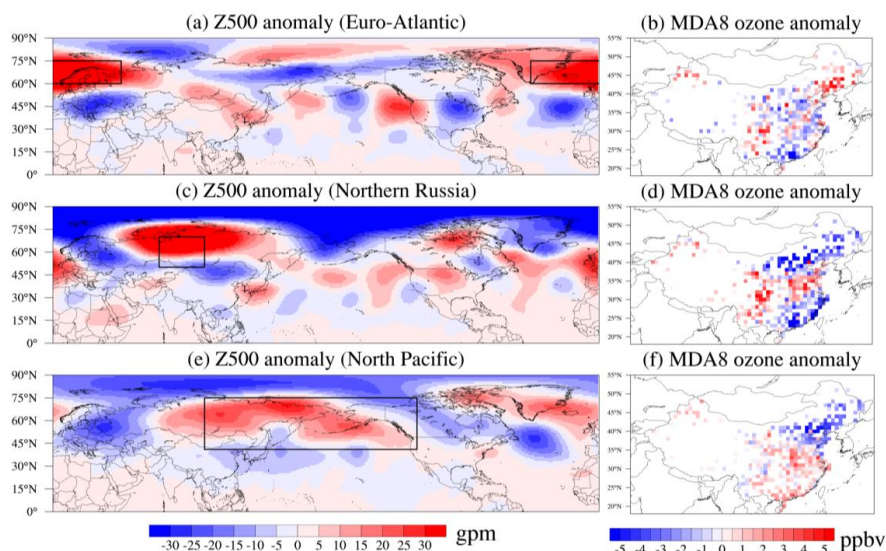
472 2020 and observed positive anomalies in summer shortwave cloud radiative effects over
473 northern Russia, promoting the generation of Ural blocking. This blocking dynamically
474 triggered a positive Eurasian pattern characterized by a “+ – +” wave train, resulting in
475 positive precipitation anomalies in northern China and strong heatwaves in southern
476 China. In addition to northwest Europe and northern Russia, blocking also occurs over
477 northeastern Russia. This, combined with the land-sea temperature contrast between
478 warm northeastern Eurasia and the colder Oyashio region in the North Pacific, may
479 induce a north–south-tilting anticyclone, leading to increased temperatures across a
480 wide area of China (Amano et al., 2023).

481 Blocking events are categorized into Euro-Atlantic, northern Russia, and North
482 Pacific regions (Fig. 7), based on their geographical locations. Analysis of NCEP
483 reanalysis data during the summers of 2015-2019 identified a total of 227 blocking days
484 in the Northern Hemisphere, with approximately 50% occurrence. Of these, 60 days
485 occurred over the Euro-Atlantic sector, 68 days over northern Russia, and 162 days over
486 the North Pacific. The higher frequency of blocking in the North Pacific is partly due
487 to conducive conditions in northeastern Russia and Alaska. Notably, the sum of
488 blocking events across these regions exceeds the total for the Northern Hemisphere,
489 owing to concurrent events in multiple areas. High blocking frequency has previously
490 been reported (Lupo, 2021), indicating climatologically in the Northern Hemisphere
491 there are 30-35 blocking events per year with a mean duration of 9 days. This
492 occurrence rate is higher than in our study, partly due to the larger frequency in winter
493 and fall compared to summer.

494 Anomalies of 500 hPa geopotential height from reanalysis data and MDA8 ozone
495 from observations during composite blocking events over Euro-Atlantic, northern
496 Russia, and North Pacific are depicted in Fig. 7. These illustrations highlight the
497 characteristics of Rossby wave propagation and the corresponding variations in ozone.
498 For instance, when blocking occurs over the Euro-Atlantic (top of Fig. 7), it coincides
499 with anomalously high pressure, triggering a wave number of 5 and resulting in high
500 pressure over northern China. This configuration leads to high ozone anomalies over



501 northeastern China, with scattered spots of high ozone anomalies over parts of North
502 China and central eastern China. When blocking shifts eastward to northern Russia
503 (middle row in Fig. 7), a positive Eurasian pattern emerges with a “+ – +” wave train.
504 This pattern manifests in negative anomalies in the northern flank of China and positive
505 pressure anomalies in central to southern eastern China, South Korea, and southern
506 Japan. During blocking over the North Pacific, spanning northeastern Russia and
507 Alaska (Fig. 7e), broad positive anomalies are observed in southern China. However,
508 notable anomalies of 500 hPa geopotential height are absent in southern China, and
509 positive high pressure is not always accompanied during ozone pollution events (Yang
510 et al., 2024).



511

512 **Fig. 7 Spatial distributions of anomalies in 500 hPa geopotential height (gpm) and**
513 **ozone.** Shown are composited results during blocking events over Euro-Atlantic sector
514 (top), northern Russia (middle), and the North Pacific (bottom), indicated by the black
515 square.

516

517 To further elucidate the pathway of Rossby wave propagation, we focus on a typical
518 blocking event from June 27 to July 4, 2019. During this period, a blocking high is
519 situated over northern Russia and the eastern flank of the Ural Mountains (Fig. 8a).



520 Coincidentally, another blocking event (June 29 - July 4, 2019) occurs over the North
521 Pacific near Alaska. regions with convergence of wave activity flux indicate weakened
522 westerlies, suggesting an incoming wave train and accumulation of wave activity in
523 these areas. This accumulation could further amplify the blocking high (Nakamura et
524 al., 1997; Schneidereit et al., 2012), serving as a source region for Rossby wave
525 propagation.

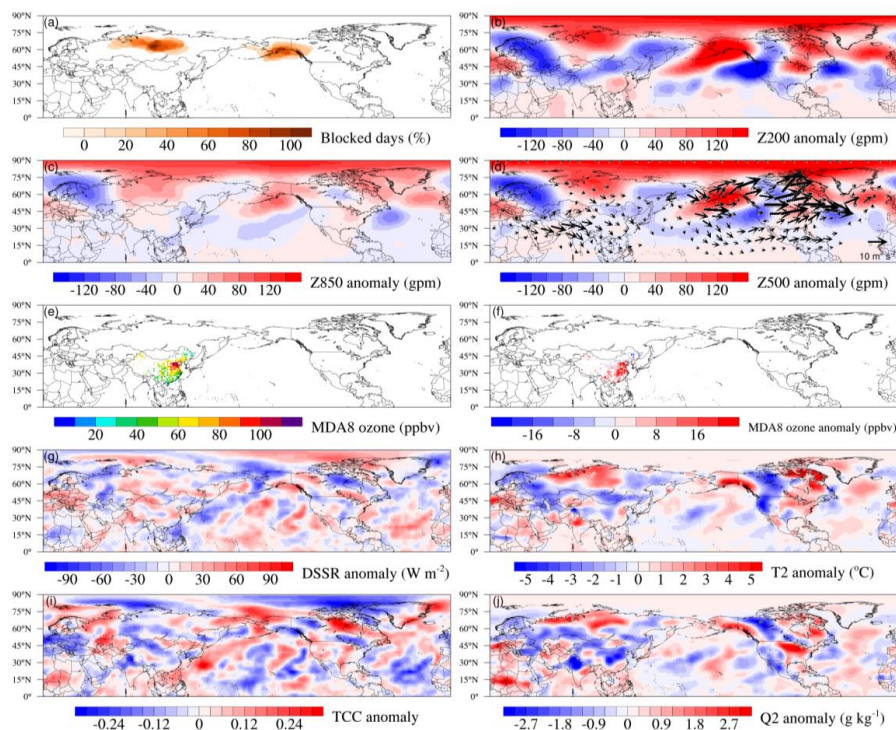
526 A strong high-pressure system over northern Russia (Fig. 8a), propagating
527 southeastward (arrows in Fig. 8d). This propagation stimulates positive height
528 anomalies over central eastern China, evident in both the upper (200 hPa; Fig. 8b) and
529 mid-troposphere (500 hPa; Fig. 8d), with a weaker signal observed at the lower
530 troposphere (850 hPa; Fig. 8c), indicating a barotropic structure (Barriopedro et al.,
531 2006; Sui et al., 2022). The blocking events over northern Russia may originate from
532 the North Atlantic, as indicated by (Liu et al., 2022). This is suggested by the presence
533 of a positive geopotential height anomaly over the northern North Atlantic, which then
534 propagates northeastward towards northern Europe and Russia. This pattern resembles
535 the Rossby wave train with a zonal wavenumber of 5, as described in Xu et al. (2019).
536 It originates west of the British Isles and propagates towards Lake Baikal, simulating a
537 high-pressure system on the southern flank of China. The blocking over Alaska serves
538 as another source of Rossby waves, propagating eastward towards the Atlantic and
539 triggering another pathway through the Mediterranean Sea along the subtropical jet.
540 This process further enhances high-pressure anomalies over central eastern China (Fig.
541 8d).

542 Modulated by this large-scale circulation, there is an increase in downward surface
543 solar radiation, 2-m air temperature, reduced water vapor, and total cloud cover over
544 areas spanning 25° to 40°N (Fig. 8g-j). These conditions contribute to widespread
545 ozone increases in this region, extending slightly into North China and southern China
546 (Fig. 8e,f). Comparably, when atmospheric blocking occurs over Euro-Atlantic region,
547 a Rossby wave propagates southeastward from the northern Atlantic. This triggers high
548 pressure anomalies in North China and central eastern China, creating meteorological



549 conditions that favor anomalously high ozone concentrations (July 20 - 24, 2017, Fig.
550 S6). Additionally, a concurrent blocking event over the North Pacific initiates another
551 Rossby wave propagation, which converges with the Rossby wave originating from the
552 Euro-Atlantic blocking. This convergence reinforces the eastward propagation of the
553 Rossby wave.

554



555

556 **Fig. 8 Spatial distribution of blocking, ozone and geopotential height.** Shown are
557 results of anomalies of geopotential height at (b), 200 hPa, (c) 850 hPa, (d) 500 hPa, (e)
558 ozone concentrations, anomalies of (f) ozone, (g), DSSR, (h) 2-m air temperature, (i)
559 total cloud cover and (j) 2-m specific humidity. The results are composited during a
560 specific blocking event over northern Russia.

561

562 Next, we explore how atmospheric blocking influences ozone through the effect of
563 BVOC emissions. In a previous study, significant improvements in summer blocking
564 simulations were achieved by increasing horizontal resolution in an Earth system model



565 with coupled atmosphere and ocean components (Gao et al., in review-a). Driven by
566 the prescribed SST, high-resolution simulations have shown enhanced blocking
567 frequencies, particularly over the Ural Mountains and North Pacific (Fig. S7).
568 Therefore, the analysis below is based solely on SW-HRESM.

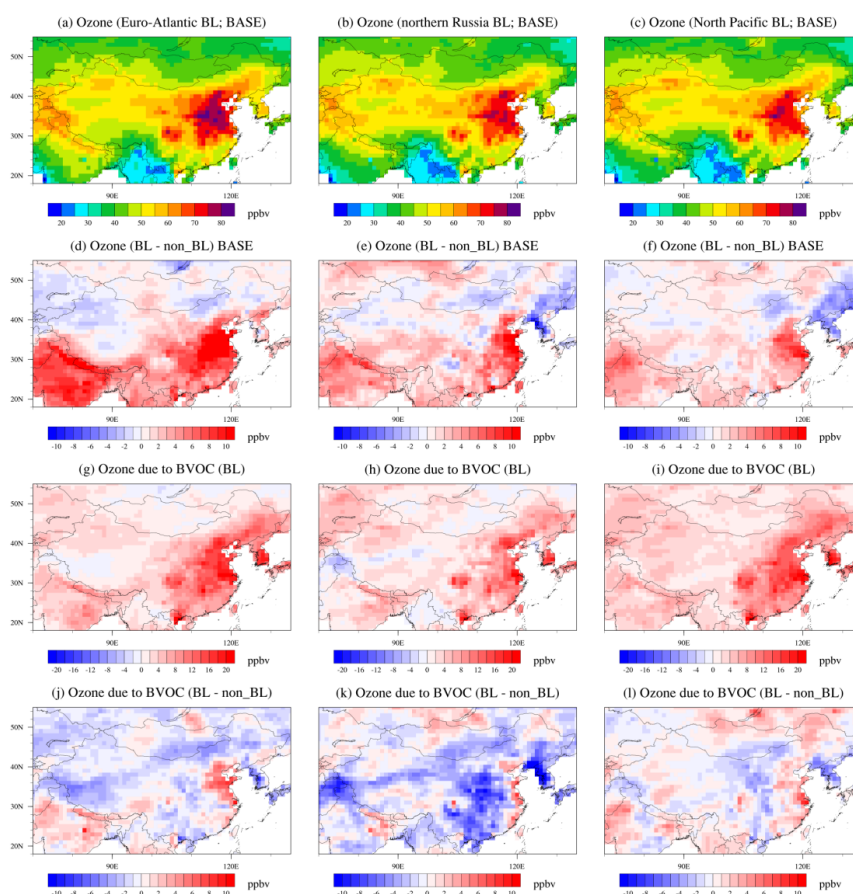
569 We composite blocking events occurring over the Euro-Atlantic sector (100 days),
570 northern Russia (47 days) and North Pacific (119 days), and the spatial distribution of
571 ozone concentrations is shown in Fig. 9. The probability distribution function of ozone
572 concentrations is shown in Fig. 10. Several distinctive features emerge. During non-
573 blocking periods (Fig. S8a; Fig. 10), the mean ozone concentrations over North China
574 is slightly higher (66.3 ppbv) than in central eastern China (63.3 ppbv). Among all three
575 blocking categories, ozone concentrations over central eastern China tend to increase
576 to a larger extent compared to North China, resulting in comparable or higher ozone
577 concentration in central eastern China relative to North China (Fig. 9d,e,f). Specifically,
578 blocking triggers an ozone increases of 10.7 ppbv, 7.1 and 5.9 ppbv when blocking
579 occurs in the Euro-Atlantic, northern Russia and North Pacific sectors, respectively,
580 compared to values of 4.9 ppbv, 4.2 ppbv and 2.1 ppbv in North China (Fig. 10). When
581 blocking occurs in northern Russia and the North Pacific, the effect can extend further
582 south from central to southeastern China. Accompanied by the blocking, an increase in
583 downward surface solar radiation, 2-m air temperature, along with reduced water vapor,
584 and total cloud cover, emerges primarily over North China and central eastern China
585 (Fig. S9). Despite slight differences, this feature is consistent with the observed patterns
586 (Fig. 7b,d,f).

587 BVOC emissions play important roles in modulating ozone concentrations. When
588 the blocking occurs, the effects of BVOC emissions on ozone concentrations range
589 from 10.6 ppbv to 15.5 ppbv over North China and central eastern China (Fig. 9g,h,i;
590 Fig. 10), with the largest effect when blocking occurs over the Euro-Atlantic sector.
591 Consistent with the previous discussion on heatwaves (section 3.3), BVOC emissions
592 play a role even in the absence of blocking (Fig. S8b), with effects of 10.8 ppbv over
593 North China and 13.3 ppbv over central eastern China. The effect of BVOC emission



594 on ozone during blocking is larger than during non-blocking for most cases, except over
595 central eastern China during blocking in northern Russia, which is visible when
596 blocking is compared to a lower temperature range (i.e., $< 26^{\circ}\text{C}$; Fig. S10). Overall, the
597 incremental effect of BVOC emissions on ozone during blocking, similar to that defined
598 in section 3.3, is calculated, and it could reach account for as much as 65% of the ozone
599 increase during blocking in North China 31% of the ozone increase during blocking in
600 central eastern China (Fig. 9j,k,l vs. Fig. 9g,h,i; Fig. 10).

601

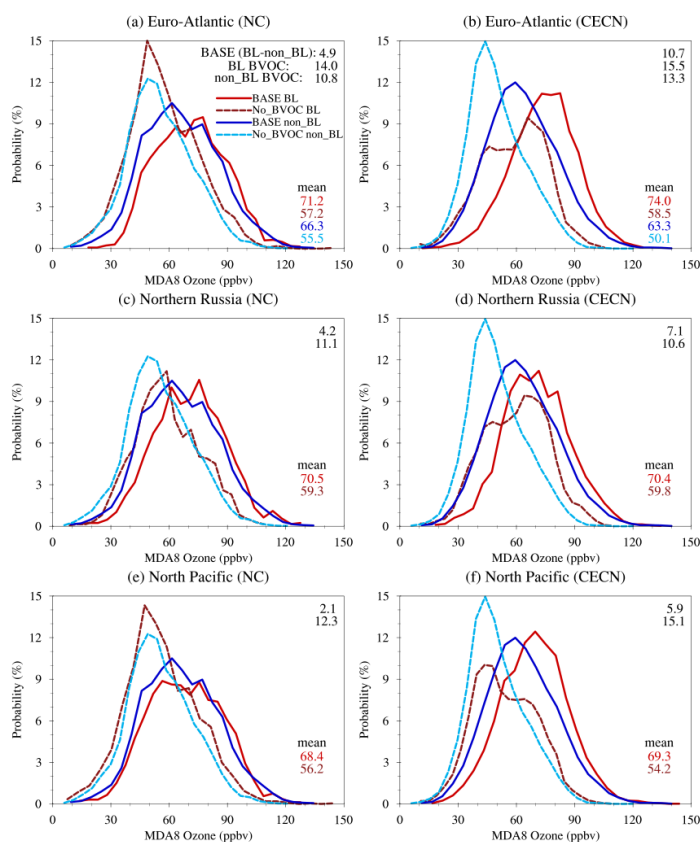


602

603 **Fig. 9 Spatial distributions of ozone concentrations.** Shown are results during
604 blocking over Euro-Atlantic (left column), northern Russia (middle column) and North
605 Pacific (right column) for (a,b,c) BASE, (d,e,f) ozone difference between blocking and



606 non-blocking, (g,h,i) effect of BVOC emissions, (j,k,l) differences of effects of BVOC
607 emissions on ozone between blocking and non-blocking.
608



609 **Fig. 10 Probability distribution function of MDA8 ozone concentrations.** Shown
610 are results over North China (NC; left column) and central eastern China (CECN; right
611 column) during blocking events occurred at Euro-Atlantic sector (top), northern Russia
612 (middle) and North Pacific (bottom). The numbers on the top right of each panel
613 represent the MDA8 ozone enhancement between blocking and non-blocking (BASE
614 (BL-non_BL)), effect of BVOC emissions during blocking (BL BVOC) and non-
615 blocking (non_BL BVOC). The numbers on the bottom right of each panel show the
616 mean MDA8 ozone concentrations during blocking (in red) and non-blocking (in blue)
617 for BASE and the case without BVOC emissions. Since ozone values in the non-
618 blocking case is the same no matter where the blocking is, values for the non-blocking
619



620 case are only listed on the top row. The solid and dashed blue lines are the same between
621 middle, bottom rows and the top row.

622

623 **Conclusions**

624 Through the combination of high-resolution Earth system models and observations,
625 the effects of local meteorology and large-scale circulation on ozone concentrations are
626 elucidated. Based on observations and focusing on eastern China, we identify that
627 ozone pollution events are accompanied by anomalously high near-surface air
628 temperature, increased downward surface solar radiation, reduced water vapor and
629 decreased total cloud cover. We further find that blocking events over the Euro-Atlantic
630 sector, northern Russia and the North Pacific behave differently in modulating ozone
631 pollution in eastern China, controlled by the pathways of Rossby wave propagation.
632 While blocking in all three regions plays the most significant role in central eastern
633 China, blocking over northern Russia and the North Pacific may also impact the
634 southern part of China. Over the North Pacific, the large high-pressure system seems to
635 form a saddle-like structure, affecting widespread areas in southern China.

636 Moreover, blocking events could substantially trigger BVOC emission increases
637 and aggravate ozone pollution. Numerical experiments reveal that under favorable
638 meteorological conditions, such as heatwaves, BVOC emissions could play an even
639 larger role in triggering ozone increases, particularly in areas with lower anthropogenic
640 emissions. This highlights a potentially more critical role for BVOC emissions,
641 especially when anthropogenic emissions are projected to decrease. This is the first
642 attempt to link atmospheric blocking, BVOC emissions, and ozone pollution, which has
643 important implications for future studies, particularly those associated with the
644 mechanisms of how large-scale circulations affect ozone concentrations under a
645 warming climate.

646

647

648



649 **Data availability.** The CESM model output data are available from the iHESP data
650 portal ([https://ihesp.github.io/archive/products/ihesp-products/data-](https://ihesp.github.io/archive/products/ihesp-products/data-release/DataRelease_Phase2.html)
651 [release/DataRelease_Phase2.html](https://ihesp.github.io/archive/products/ihesp-products/data-release/DataRelease_Phase2.html)).

652 **Author contributions**

653 Y.G. conceived the project and designed the method, W.K. performed the analysis and
654 drafted the manuscript, X.G., X.A. helped on the analysis, D.T, W.L., M.C., X.G., S.Z.,
655 H.G., L.W. helped on the interpretation of the results. All authors contributed to the
656 writing of the manuscript.

657

658 **Competing interests**

659 The authors declare that they have no conflicts of interest.

660

661

662 **Acknowledgements**

663 This work was supported by the National Natural Science Foundation of China
664 (42122039, 42375189), the Science and Technology Innovation Project of Laoshan
665 Laboratory (LSKJ202300401, LSKJ202202201) and Hainan Provincial Joint Project of
666 Sanya Yazhou Bay Science and Technology City (2021JLH0050).

667

668 **References**

669 Amano, M., Tachibana, Y., and Ando, Y.: Consideration of whether a climatic regime shift has prevented
670 the occurrence of a cold summer in northeast Eurasia since 2010, *Journal of Climate*, 10.1175/jcli-d-23-
671 0191.1, 2023.

672 Barnes, E. A., and Fiore, A. M.: Surface ozone variability and the jet position: Implications for projecting
673 future air quality, *Geophysical Research Letters*, 40, 2839-2844, 10.1002/grl.50411, 2013.

674 Barriopedro, D., García-Herrera, R., Lupo, A. R., and Hernández, E.: A Climatology of Northern
675 Hemisphere Blocking, *Journal of Climate*, 19, 1042-1063, 10.1175/JCLI3678.1, 2006.

676 Barriopedro, D., Fischer, E. M., Luterbacher, J., Trigo, R., and Garcia-Herrera, R.: The Hot Summer of
677 2010: Redrawing the Temperature Record Map of Europe, *Science*, 332, 220-224,
678 10.1126/science.1201224, 2011.

679 Brauer, M., Casadei, B., Harrington, R. A., Kovacs, R., Sliwa, K., and Grp, W. A. P. E.: Taking a stand



- 680 against air pollution - the impact on cardiovascular disease, *European Heart Journal*, 42, 1460-1463,
681 10.1093/eurheartj/ehaa1025, 2021.
- 682 Cattiaux, J., Vautard, R., Cassou, C., Yiou, P., Masson-Delmotte, V., and Codron, F.: Winter 2010 in
683 Europe: A cold extreme in a warming climate, *Geophysical Research Letters*, 37, 10.1029/2010gl044613,
684 2010.
- 685 Chang, P., Zhang, S., Danabasoglu, G., Yeager, S. G., Fu, H., Wang, H., Castruccio, F. S., Chen, Y.,
686 Edwards, J., Fu, D., Jia, Y., Laurindo, L. C., Liu, X., Rosenbloom, N., Small, R. J., Xu, G., Zeng, Y.,
687 Zhang, Q., Bacmeister, J., Bailey, D. A., Duan, X., DuVivier, A. K., Li, D., Li, Y., Neale, R., Stössel, A.,
688 Wang, L., Zhuang, Y., Baker, A., Bates, S., Dennis, J., Diao, X., Gan, B., Gopal, A., Jia, D., Jing, Z., Ma,
689 X., Saravanan, R., Strand, W. G., Tao, J., Yang, H., Wang, X., Wei, Z., and Wu, L.: An Unprecedented
690 Set of High-Resolution Earth System Simulations for Understanding Multiscale Interactions in Climate
691 Variability and Change, *Journal of Advances in Modeling Earth Systems*, 12, e2020MS002298,
692 10.1029/2020MS002298, 2020.
- 693 Christoudias, T., Pozzer, A., and Lelieveld, J.: Influence of the North Atlantic Oscillation on air pollution
694 transport, *Atmos. Chem. Phys.*, 12, 869-877, 10.5194/acp-12-869-2012, 2012.
- 695 Churkina, G., Kuik, F., Bonn, B., Lauer, A., Grote, R., Tomiak, K., and Butler, T. M.: Effect of VOC
696 Emissions from Vegetation on Air Quality in Berlin during a Heatwave, *Environmental Science &
697 Technology*, 51, 6120-6130, 10.1021/acs.est.6b06514, 2017.
- 698 Clifton, O. E., Fiore, A. M., Massman, W. J., Baublitz, C. B., Coyle, M., Emberson, L., Fares, S., Farmer,
699 D. K., Gentine, P., Gerosa, G., Guenther, A. B., Helmig, D., Lombardozzi, D. L., Munger, J. W., Patton,
700 E. G., Pusede, S. E., Schwede, D. B., Silva, S. J., Sörgel, M., Steiner, A. L., and Tai, A. P. K.: Dry
701 Deposition of Ozone Over Land: Processes, Measurement, and Modeling, *Reviews of Geophysics*, 58,
702 e2019RG000670, 10.1029/2019RG000670, 2020.
- 703 Deitrick, R., and Goldblatt, C.: Effects of ozone levels on climate through Earth history, *Climate of the
704 Past*, 19, 1201-1218, 10.5194/cp-19-1201-2023, 2023.
- 705 Dentener, F., Keating, T., and Akimoto, H.: Hemispheric transport of air pollution 2010, Part A - Ozone
706 and Particulate Matter, *Air Pollution Studies No.17*. United Nations, New York and Geneva, 2010.
- 707 Ding, F., and Li, C.: Subtropical westerly jet waveguide and winter persistent heavy rainfall in south
708 China, *Journal of Geophysical Research: Atmospheres*, 122, 7385-7400, 10.1002/2017JD026530, 2017.
- 709 Dunker, A. M., Koo, B., and Yarwood, G.: Contributions of foreign, domestic and natural emissions to
710 US ozone estimated using the path-integral method in CAMx nested within GEOS-Chem, *Atmospheric
711 Chemistry and Physics*, 17, 12553-12571, 10.5194/acp-17-12553-2017, 2017.
- 712 Emberson, L. D., Pleijel, H., Ainsworth, E. A., van den Berg, M., Ren, W., Osborne, S., Mills, G., Pandey,
713 D., Dentener, F., Büker, P., Ewert, F., Koeble, R., and Van Dingenen, R.: Ozone effects on crops and
714 consideration in crop models, *European Journal of Agronomy*, 100, 19-34, 10.1016/j.eja.2018.06.002,
715 2018.



- 716 Emmons, L. K., Schwantes, R. H., Orlando, J. J., Tyndall, G., Kinnison, D., Lamarque, J.-F., Marsh, D.,
717 Mills, M. J., Tilmes, S., Bardeen, C., Buchholz, R. R., Conley, A., Gettelman, A., Garcia, R., Simpson,
718 I., Blake, D. R., Meinardi, S., and Pétron, G.: The Chemistry Mechanism in the Community Earth System
719 Model Version 2 (CESM2), *Journal of Advances in Modeling Earth Systems*, 12, e2019MS001882,
720 10.1029/2019MS001882, 2020.
- 721 Fu, T.-M., and Tian, H.: Climate Change Penalty to Ozone Air Quality: Review of Current
722 Understandings and Knowledge Gaps, *Current Pollution Reports*, 5, 159-171, 10.1007/s40726-019-
723 00115-6, 2019.
- 724 Fuller, R., Landrigan, P. J., Balakrishnan, K., Bathan, G., Bose-O'Reilly, S., Brauer, M., Caravanos, J.,
725 Chiles, T., Cohen, A., Corra, L., Cropper, M., Ferraro, G., Hanna, J., Hanrahan, D., Hu, H., Hunter, D.,
726 Janata, G., Kupka, R., Lanphear, B., Lichtveld, M., Martin, K., Mustapha, A., Sanchez-Triana, E.,
727 Sandilya, K., Schaeffli, L., Shaw, J., Seddon, J., Suk, W., Téllez-Rojo, M. M., and Yan, C. H.: Pollution
728 and health: a progress update, *Lancet Planetary Health*, 6, E535-E547, 10.1016/S2542-5196(22)00090-
729 0, 2022.
- 730 Gao, Y., Fu, J. S., Drake, J. B., Liu, Y., and Lamarque, J. F.: Projected changes of extreme weather events
731 in the eastern United States based on a high resolution climate modeling system, *Environmental Research*
732 *Letters*, 7, 044025, 10.1088/1748-9326/7/4/044025, 2012.
- 733 Gao, Y., Zhang, J. X., Yan, F. F., Leung, L. R., Luo, K., Zhang, Y., and Bell, M. L.: Nonlinear effect of
734 compound extreme weather events on ozone formation over the United States, *Weather and Climate*
735 *Extremes*, 30, 100285, 10.1016/j.wace.2020.100285, 2020.
- 736 Gao, Y., Yan, F., Ma, M., Ding, A., Liao, H., Wang, S., Wang, X., Zhao, B., Cai, W., Su, H., Yao, X., and
737 Gao, H.: Unveiling the dipole synergic effect of biogenic and anthropogenic emissions on ozone
738 concentrations, *Science of The Total Environment*, 818, 151722, 10.1016/j.scitotenv.2021.151722, 2022.
- 739 Gao, Y., Wu, Y., Guo, X., Kou, W., Zhang, S., Leung, L. R., Chen, X., Lu, J., Diffenbaugh, N. S., Horton,
740 D. E., Yao, X., Gao, H., and Wu, L.: More Frequent and Persistent Heatwaves Due To Increased
741 Temperature Skewness Projected by a High-Resolution Earth System Model, *Geophysical Research*
742 *Letters*, 50, e2023GL105840, 10.1029/2023GL105840, 2023.
- 743 Gao, Y., Guo, X., Lu, J., Woolings, T., Chen, D., Guo, X., Kou, W., Zhang, S., Leung, L. R., Schiemann,
744 R., Turner, A., O'Reilly, C., Guo, C., Li, J., Gao, H., and Wu, L.: Enhanced Simulation of Atmospheric
745 Blocking with High-Resolution Earth System Models: Implications for Future Climate Scenarios, in
746 review-a.
- 747 Gao, Y., Kou, W., Cheng, W., Guo, X., Qu, B., Wu, Y., Zhang, S., Liao, H., Chen, D., Leung, L. R., Wild,
748 O., Zhang, J., Lin, G., Su, H., Cheng, Y., Pöschl, U., Pozzer, A., Zhang, L., Lamarque, J.-F., Guenther, A.
749 B., Brasseur, G., Liu, Z., Lu, H., Li, C., Zhao, B., Wang, S., Huang, X., Pan, J., Liu, G., Liu, X., Lin, H.,
750 Zhao, Y., Zhao, C., Meng, J., Yao, X., Gao, H., and Wu, L.: Reducing long-standing surface ozone
751 overestimation in Earth system modelling by high-resolution simulation and dry deposition improvement,
752 in review-b.



- 753 Gong, C., and Liao, H.: A typical weather pattern for ozone pollution events in North China, *Atmos.*
754 *Chem. Phys.*, 19, 13725-13740, 10.5194/acp-19-13725-2019, 2019.
- 755 Gong, C., Liao, H., Zhang, L., Yue, X., Dang, R., and Yang, Y.: Persistent ozone pollution episodes in
756 North China exacerbated by regional transport, *Environmental Pollution*, 265, 115056,
757 10.1016/j.envpol.2020.115056, 2020.
- 758 Granier, C., Darras, S., Gon, H. D. v. d., Doubalova, J., Elguindi, N., Galle, B., M. Gauss, M., and
759 Guevara, J.-P. J., J. Kuenen, C. Lioussé, B. Quack, D. Simpson, K. Sindelarova, : The Copernicus
760 Atmosphere Monitoring Service global and regional emissions (April 2019 version), Copernicus
761 Atmosphere Monitoring Service (CAMS) report, 10.24380/d0bn-kx16, 2019.
- 762 Guenther, A. B., Jiang, X., Heald, C. L., Sakulyanontvittaya, T., Duhl, T., Emmons, L. K., and Wang, X.:
763 The Model of Emissions of Gases and Aerosols from Nature version 2.1 (MEGAN2.1): an extended and
764 updated framework for modeling biogenic emissions, *Geoscientific Model Development*, 5, 1471-1492,
765 10.5194/gmd-5-1471-2012, 2012.
- 766 Guion, A., Turquety, S., Cholakian, A., Polcher, J., Ehret, A., and Lathiere, J.: Biogenic isoprene
767 emissions, dry deposition velocity, and surface ozone concentration during summer droughts, heatwaves,
768 and normal conditions in southwestern Europe, *Atmospheric Chemistry and Physics*, 23, 1043-1071,
769 10.5194/acp-23-1043-2023, 2023.
- 770 Guo, X., Gao, Y., Zhang, S., Wu, L., Chang, P., Cai, W., Zscheischler, J., Leung, L. R., Small, J.,
771 Danabasoglu, G., Thompson, L., and Gao, H.: Threat by marine heatwaves to adaptive large marine
772 ecosystems in an eddy-resolving model, *Nature Climate Change*, 12, 179-186, 10.1038/s41558-021-
773 01266-5, 2022.
- 774 Kalnay, E., Kanamitsu, M., Kistler, R., Collins, W., Deaven, D., Gandin, L., Iredell, M., Saha, S., White,
775 G., Woollen, J., Zhu, Y., Chelliah, M., Ebisuzaki, W., Higgins, W., Janowiak, J., Mo, K. C., Ropelewski,
776 C., Wang, J., Leetmaa, A., Reynolds, R., Jenne, R., and Joseph, D.: The NCEP/NCAR 40-Year Reanalysis
777 Project, *Bulletin of the American Meteorological Society*, 77, 437-472, 10.1175/1520-
778 0477(1996)077<0437:TNYRP>2.0.CO;2, 1996.
- 779 Kang, D. W., Aneja, V. P., Mathur, R., and Ray, J. D.: Nonmethane hydrocarbons and ozone in three rural
780 southeast United States national parks: A model sensitivity analysis and comparison to measurements,
781 *Journal of Geophysical Research-Atmospheres*, 108, 4604, 10.1029/2002jd003054, 2003.
- 782 Lamarque, J. F., Emmons, L. K., Hess, P. G., Kinnison, D. E., Tilmes, S., Vitt, F., Heald, C. L., Holland,
783 E. A., Lauritzen, P. H., Neu, J., Orlando, J. J., Rasch, P. J., and Tyndall, G. K.: CAM-chem: description
784 and evaluation of interactive atmospheric chemistry in the Community Earth System Model, *Geosci.*
785 *Model Dev.*, 5, 369-411, 10.5194/gmd-5-369-2012, 2012.
- 786 Li, M., Liu, H., Geng, G. N., Hong, C. P., Liu, F., Song, Y., Tong, D., Zheng, B., Cui, H. Y., Man, H. Y.,
787 Zhang, Q., and He, K. B.: Anthropogenic emission inventories in China: a review, *National Science*
788 *Review*, 4, 834-866, 10.1093/nsr/nwx150, 2017.
- 789 Li, R.-X., and Sun, J.-Q.: Interdecadal variability of the large-scale extreme hot event frequency over the



- 790 middle and lower reaches of the Yangtze River basin and its related atmospheric patterns, *Atmospheric*
791 *and Oceanic Science Letters*, 11, 63-70, 10.1080/16742834.2017.1335580, 2018.
- 792 Liu, L., Wu, B., and Ding, S.: On the Association of the Summertime Shortwave Cloud Radiative Effect
793 in Northern Russia With Atmospheric Circulation and Climate Over East Asia, *Geophysical Research*
794 *Letters*, 49, e2021GL096606, 10.1029/2021GL096606, 2022.
- 795 Lupo, A. R.: Atmospheric blocking events: a review, *Annals of the New York Academy of Sciences*, 1504,
796 5-24, 10.1111/nyas.14557, 2021.
- 797 Ma, M., Gao, Y., Ding, A., Su, H., Liao, H., Wang, S., Wang, X., Zhao, B., Zhang, S., Fu, P., Guenther,
798 A. B., Wang, M., Li, S., Chu, B., Yao, X., and Gao, H.: Development and Assessment of a High-
799 Resolution Biogenic Emission Inventory from Urban Green Spaces in China, *Environmental Science &*
800 *Technology*, 56, 175-184, 10.1021/acs.est.1c06170, 2022.
- 801 Ma, M. C., Gao, Y., Wang, Y. H., Zhang, S. Q., Leung, L. R., Liu, C., Wang, S. X., Zhao, B., Chang, X.,
802 Su, H., Zhang, T. Q., Sheng, L. F., Yao, X. H., and Gao, H. W.: Substantial ozone enhancement over the
803 North China Plain from increased biogenic emissions due to heat waves and land cover in summer 2017,
804 *Atmospheric Chemistry and Physics*, 19, 12195-12207, 10.5194/acp-19-12195-2019, 2019.
- 805 Masato, G., Hoskins, B. J., and Woollings, T.: Winter and Summer Northern Hemisphere Blocking in
806 CMIP5 Models, *Journal of Climate*, 26, 7044-7059, 10.1175/JCLI-D-12-00466.1, 2013.
- 807 Meehl, G. A., Tebaldi, C., Tilmes, S., Lamarque, J. F., Bates, S., Pendergrass, A., and Lombardozzi, D.:
808 Future heat waves and surface ozone, *Environmental Research Letters*, 13, 064004, 10.1088/1748-
809 9326/aabedc, 2018.
- 810 Mochizuki, T., Ikeda, F., and Tani, A.: Effect of growth temperature on monoterpene emission rates of
811 *Acer palmatum*, *Science of the Total Environment*, 745, 140886, 10.1016/j.scitotenv.2020.140886, 2020.
- 812 Mousavinezhad, S., Choi, Y., Pouyaei, A., Ghahremanloo, M., and Nelson, D. L.: A comprehensive
813 investigation of surface ozone pollution in China, 2015–2019: Separating the contributions from
814 meteorology and precursor emissions, *Atmospheric Research*, 257, 105599,
815 10.1016/j.atmosres.2021.105599, 2021.
- 816 Nakamura, H., Nakamura, M., and Anderson, J. L.: The Role of High- and Low-Frequency Dynamics in
817 Blocking Formation, *Monthly Weather Review*, 125, 2074-2093, 10.1175/1520-
818 0493(1997)125<2074:TROHAL>2.0.CO;2, 1997.
- 819 Nuvolone, D., Petri, D., and Voller, F.: The effects of ozone on human health, *Environmental Science*
820 *and Pollution Research*, 25, 8074-8088, 10.1007/s11356-017-9239-3, 2018.
- 821 Opacka, B., Müller, J. F., Stavrakou, T., Bauwens, M., Sindelarova, K., Markova, J., and Guenther, A.
822 B.: Global and regional impacts of land cover changes on isoprene emissions derived from spaceborne
823 data and the MEGAN model, *Atmospheric Chemistry and Physics*, 21, 8413-8436, 10.5194/acp-21-
824 8413-2021, 2021.



- 825 Parrish, D. D., Law, K. S., Staehelin, J., Derwent, R., Cooper, O. R., Tanimoto, H., Volz-Thomas, A.,
826 Gilge, S., Scheel, H. E., Steinbacher, M., and Chan, E.: Long-term changes in lower tropospheric baseline
827 ozone concentrations at northern mid-latitudes, *Atmospheric Chemistry and Physics*, 12, 11485-11504,
828 10.5194/acp-12-11485-2012, 2012.
- 829 Parrish, D. D., Derwent, R. G., and Faloon, I. C.: Long-term baseline ozone changes in the Western US:
830 A synthesis of analyses, *Journal of the Air & Waste Management Association*, 71, 1397-1406,
831 10.1080/10962247.2021.1945706, 2021a.
- 832 Parrish, D. D., Derwent, R. G., and Staehelin, J.: Long-term changes in northern mid-latitude
833 tropospheric ozone concentrations: Synthesis of two recent analyses, *Atmospheric Environment*, 248,
834 118227, 10.1016/j.atmosenv.2021.118227, 2021b.
- 835 Pelly, J. L., and Hoskins, B. J.: A new perspective on blocking, *Journal of the Atmospheric Sciences*, 60,
836 743-755, 10.1175/1520-0469(2003)060<0743:Anpob>2.0.Co;2, 2003.
- 837 Pugh, T. A. M., Ashworth, K., Wild, O., and Hewitt, C. N.: Effects of the spatial resolution of climate
838 data on estimates of biogenic isoprene emissions, *Atmospheric Environment*, 70, 1-6,
839 10.1016/j.atmosenv.2013.01.001, 2013.
- 840 Schneidereit, A., Schubert, S., Vargin, P., Lunkeit, F., Zhu, X., Peters, D. H. W., and Fraedrich, K.: Large-
841 Scale Flow and the Long-Lasting Blocking High over Russia: Summer 2010, *Monthly Weather Review*,
842 140, 2967-2981, 10.1175/MWR-D-11-00249.1, 2012.
- 843 Schwierz, C., Croci-Maspoli, M., and Davies, H. C.: Perspicacious indicators of atmospheric blocking,
844 *Geophysical Research Letters*, 31, 10.1029/2003gl019341, 2004.
- 845 Sillmann, J., Kharin, V. V., Zhang, X., Zwiers, F. W., and Bronaugh, D.: Climate extremes indices in the
846 CMIP5 multimodel ensemble: Part I. Model evaluation in the present climate, *Journal of Geophysical
847 Research: Atmospheres*, 118, 1716-1733, 10.1002/jgrd.50203, 2013.
- 848 Sui, C., Karpechko, A. Y., Vihma, T., Yu, L., and Feng, L.: Influence of the Ural High on Air Temperatures
849 over Eastern Europe and Northern China during Extended Winter, *Journal of Climate*, 35, 1309-1325,
850 10.1175/JCLI-D-21-0523.1, 2022.
- 851 Sun, W. X., Hess, P., Chen, G., and Tilmes, S.: How waviness in the circulation changes surface ozone:
852 a viewpoint using local finite-amplitude wave activity, *Atmospheric Chemistry and Physics*, 19, 12917-
853 12933, 10.5194/acp-19-12917-2019, 2019.
- 854 Takaya, K., and Nakamura, H.: A Formulation of a Phase-Independent Wave-Activity Flux for Stationary
855 and Migratory Quasigeostrophic Eddies on a Zonally Varying Basic Flow, *Journal of the Atmospheric
856 Sciences*, 58, 608-627, 10.1175/1520-0469(2001)058<0608:AFOAPI>2.0.CO;2, 2001.
- 857 Tarasick, D., Galbally, I. E., Cooper, O. R., Schultz, M. G., Ancellet, G., Leblanc, T., Wallington, T. J.,
858 Ziemke, J., Liu, X., Steinbacher, M., Staehelin, J., Vigouroux, C., Hannigan, J. W., García, O., Foret, G.,
859 Zanis, P., Weatherhead, E., Petropavlovskikh, I., Worden, H., Osman, M., Liu, J., Chang, K. L., Gaudel,
860 A., Lin, M. Y., Granados-Muñoz, M., Thompson, A. M., Oltmans, S. J., Cuesta, J., Dufour, G., Thouret,



- 861 V., Hassler, B., Trickl, T., and Neu, J. L.: Tropospheric Ozone Assessment Report: Tropospheric ozone
862 from 1877 to 2016, observed levels, trends and uncertainties, *Elementa-Science of the Anthropocene*, 7,
863 39, 10.1525/elementa.376, 2019.
- 864 Tonnesen, S., and Jeffries, H. E.: Inhibition of odd oxygen production in the carbon bond four and generic
865 reaction set mechanisms, *Atmospheric Environment*, 28, 1339-1349, 10.1016/1352-2310(94)90281-X,
866 1994.
- 867 Unger, N.: On the role of plant volatiles in anthropogenic global climate change, *Geophysical Research*
868 *Letters*, 41, 8563-8569, 10.1002/2014gl061616, 2014.
- 869 Wang, H. L., Wu, K., Liu, Y. M., Sheng, B. S., Lu, X., He, Y. P., Xie, J. L., Wang, H. C., and Fan, S. J.:
870 Role of Heat Wave-Induced Biogenic VOC Enhancements in Persistent Ozone Episodes Formation in
871 Pearl River Delta, *Journal of Geophysical Research-Atmospheres*, 126, e2020JD034317,
872 10.1029/2020JD034317, 2021.
- 873 Weng, H., Lin, J., Martin, R., Millet, D. B., Jaeglé, L., Ridley, D., Keller, C., Li, C., Du, M., and Meng,
874 J.: Global high-resolution emissions of soil NO_x, sea salt aerosols, and biogenic volatile organic
875 compounds, *Scientific Data*, 7, 148, 10.1038/s41597-020-0488-5, 2020.
- 876 Wiedinmyer, C., Kimura, Y., McDonald-Buller, E. C., Emmons, L. K., Buchholz, R. R., Tang, W., Seto,
877 K., Joseph, M. B., Barsanti, K. C., Carlton, A. G., and Yokelson, R.: The Fire Inventory from NCAR
878 version 2.5: an updated global fire emissions model for climate and chemistry applications, *Geosci.*
879 *Model Dev.*, 16, 3873-3891, 10.5194/gmd-16-3873-2023, 2023.
- 880 Woollings, T., Barriopedro, D., Methven, J., Son, S.-W., Martius, O., Harvey, B., Sillmann, J., Lupo, A.
881 R., and Seneviratne, S.: Blocking and its Response to Climate Change, *Current Climate Change Reports*,
882 4, 287-300, 10.1007/s40641-018-0108-z, 2018.
- 883 Xu, P., Wang, L., and Chen, W.: The British–Baikal Corridor: A Teleconnection Pattern along the
884 Summertime Polar Front Jet over Eurasia, *Journal of Climate*, 32, 877-896, 10.1175/JCLI-D-18-0343.1,
885 2019.
- 886 Yang, X., Zeng, G., Iyakaremye, V., and Zhu, B.: Effects of different types of heat wave days on ozone
887 pollution over Beijing-Tianjin-Hebei and its future projection, *Science of The Total Environment*, 837,
888 155762, 10.1016/j.scitotenv.2022.155762, 2022.
- 889 Yang, Y., Liao, H., and Li, J.: Impacts of the East Asian summer monsoon on interannual variations of
890 summertime surface-layer ozone concentrations over China, *Atmos. Chem. Phys.*, 14, 6867–6879,
891 10.5194/acp-14-6867-2014, 2014.
- 892 Yang, Y., Zhou, Y., Wang, H., Li, M., Li, H., Wang, P., Yue, X., Li, K., Zhu, J., and Liao, H.:
893 Meteorological characteristics of extreme ozone pollution events in China and their future predictions,
894 *Atmos. Chem. Phys.*, 24, 1177-1191, 10.5194/acp-24-1177-2024, 2024.
- 895 Yao, Y., Zhuo, W., Gong, Z., Luo, B., Luo, D., Zheng, F., Zhong, L., Huang, F., Ma, S., Zhu, C., and
896 Zhou, T.: Extreme Cold Events in North America and Eurasia in November-December 2022: A Potential



- 897 Vorticity Gradient Perspective, *Advances in Atmospheric Sciences*, 40, 953-962, 10.1007/s00376-023-
898 2384-3, 2023.
- 899 Yin, Z., Wang, H., Li, Y., Ma, X., and Zhang, X.: Links of climate variability in Arctic sea ice, Eurasian
900 teleconnection pattern and summer surface ozone pollution in North China, *Atmos. Chem. Phys.*, 19,
901 3857-3871, 10.5194/acp-19-3857-2019, 2019.
- 902 Zeng, X. R., Gao, Y., Wang, Y. H., Ma, M. C., Zhang, J. X., and Sheng, L. F.: Characterizing the distinct
903 modulation of future emissions on summer ozone concentrations between urban and rural areas over
904 China, *Science of the Total Environment*, 820, 153324, 10.1016/j.scitotenv.2022.153324, 2022.
- 905 Zhang, J., Gao, Y., Leung, L. R., Luo, K., Wang, M., Zhang, Y., Bell, M. L., and Fan, J.: Isolating the
906 modulation of mean warming and higher-order temperature changes on ozone in a changing climate over
907 the contiguous United States, *Environmental Research Letters*, 17, 094005, 10.1088/1748-9326/ac8695,
908 2022.
- 909 Zhang, J. X., Gao, Y., Luo, K., Leung, L. R., Zhang, Y., Wang, K., and Fan, J. R.: Impacts of compound
910 extreme weather events on ozone in the present and future, *Atmospheric Chemistry and Physics*, 18,
911 9861-9877, 10.5194/acp-18-9861-2018, 2018.
- 912 Zhang, R., Cohan, A., Biazar, A. P., and Cohan, D. S.: Source apportionment of biogenic contributions
913 to ozone formation over the United States, *Atmospheric Environment*, 164, 8-19,
914 10.1016/j.atmosenv.2017.05.044, 2017.
- 915 Zohdirad, H., Jiang, J. H., Aksoyoglu, S., Namin, M. M., Ashrafi, K., and Prevot, A. S. H.: Investigating
916 sources of surface ozone in central Europe during the hot summer in 2018: High temperatures, but not
917 so high ozone, *Atmospheric Environment*, 279, 119099, 10.1016/j.atmosenv.2022.119099, 2022.
- 918